



# Enhanced methane decomposition over nickel–carbon–B<sub>2</sub>O<sub>3</sub> core–shell catalysts derived from carbon dioxide

D. Kang, Jae W. Lee \*

Department of Chemical and Biomolecular Engineering, Korea Advanced Institute of Science and Technology (KAIST), Daejeon 305-701, Republic of Korea



## ARTICLE INFO

### Article history:

Received 29 July 2015

Received in revised form

28 December 2015

Accepted 29 December 2015

Available online 2 January 2016

### Keywords:

Nickel–carbon–B<sub>2</sub>O<sub>3</sub> core–shell catalysts

Catalytic methane decomposition (CMD)

Hydrogen production

Carbon nanoionons

Carbon dioxide regeneration

## ABSTRACT

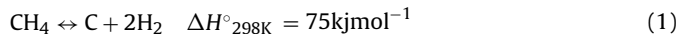
Nickel–carbon–B<sub>2</sub>O<sub>3</sub> nanocomposites (Ni@C-B<sub>2</sub>O<sub>3</sub>s) were synthesized from a single-step reaction of CO<sub>2</sub> with NaBH<sub>4</sub> at 1 bar and investigated as catalysts for methane decomposition. These catalysts exhibited an unprecedented activity for producing hydrogen and graphitic carbon nanoionons (CNOs) without any generation of carbon oxides (CO<sub>x</sub>), despite of the absence of a catalyst reduction step by hydrogen. Around 90% of methane conversion with 61 mmol min<sup>-1</sup> g<sub>Ni</sub><sup>-1</sup> was achieved using 13 wt% nickel-containing Ni@C-B<sub>2</sub>O<sub>3</sub> (13Ni@C-B<sub>2</sub>O<sub>3</sub>) at 850 °C under 46.15 L<sub>CH<sub>4</sub></sub> h<sup>-1</sup> g<sub>Ni</sub><sup>-1</sup>. The uncompromising activity of the catalyst comes from the two major contributions: the absence of nickel oxide eliminates the formation of carbon oxides and the amorphous core–shell structure of Ni@C-B<sub>2</sub>O<sub>3</sub>s facilitates nano-sized nickel cores to escape the CNOs and directly decompose methane. This was verified by various microscopic and spectroscopic investigations. The generated CNOs on 13Ni@C-B<sub>2</sub>O<sub>3</sub> were partially oxidized by CO<sub>2</sub> as a mild oxidant with the production of CO. The catalytic activity of 13Ni@C-B<sub>2</sub>O<sub>3</sub> was maintained for 15 cycles, providing a potential of enabling the cyclic process of CH<sub>4</sub> decomposition/CO<sub>2</sub> regeneration. By synthesizing Ni@C-B<sub>2</sub>O<sub>3</sub>s from CO<sub>2</sub> and using them to the cyclic operation, not only was CO<sub>2</sub> converted to the valuable catalyst, but hydrogen, CNOs, and CO were also produced from the greenhouse gases of methane and CO<sub>2</sub>.

© 2015 Elsevier B.V. All rights reserved.

## 1. Introduction

Although natural gas has been drawing many attentions as a substitute of petro- or coal-based energy, methane, a primary component of natural gas, is also ranked as a major contributor to greenhouse effects, which is equivalent to 0.6 billion tons of CO<sub>2</sub> emission [1]. The emission of methane can be reduced and the economic feasibility of the natural gas supply chain can be elevated if methane is converted to value-added products. To make the most efficient use of natural gas based energy, a lot of studies have focused on converting methane to hydrogen which has a wider range of applications [2] than the use of methane itself through diverse methods such as steam [3] or dry reforming [4–6], and partial oxidation of methane [7,8]. However, these traditional methods inevitably generate CO, CO<sub>2</sub> and H<sub>2</sub>O as byproducts. Therefore, additional purification steps are needed to produce pure hydrogen.

On the contrary, catalytic methane decomposition (CMD) is one of promising processes for converting methane to hydrogen and carbon nano-materials without using steam or O<sub>2</sub> [9–12]. CMD is a CO<sub>x</sub>-free hydrogen production process as in Eq. (1) which can save both capital and operating costs by eliminating additional product purification and water gas shift reaction steps.



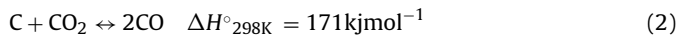
During the CMD process, the carbon deposition causes a metal to lose its catalytic activity and thus the spent catalyst should be regenerated or the carbon deposition itself should be utilized as a valuable carbon nano-material.

To regenerate the spent catalyst, the solid carbon deposition is oxidized by O<sub>2</sub>, steam, or CO<sub>2</sub>. When O<sub>2</sub> is used as a regeneration gas, the metal in the catalyst is oxidized to its oxide form, resulting in the production of CO<sub>x</sub>-byproducts during the next CMD step [13–15]. In the case of steam regeneration, mixtures of CO<sub>x</sub> and hydrogen are inevitably produced during the regeneration step, so that the purification step is required to recover the pure products [13,16–18]. When the carbon deposition is oxidized by CO<sub>2</sub> in Eq. (2), high-purity CO and hydrogen are produced during the regeneration and the next CMD step, respectively [19–22], thus CO<sub>2</sub> can

\* Corresponding author. Fax: +82 42 350 3910.

E-mail address: [jaewlee@kaist.ac.kr](mailto:jaewlee@kaist.ac.kr) (J.W. Lee).

be considered as a promising reagent for regenerating the spent catalyst.



Among the reported forms of carbon nano-material [11], carbon nanonion (CNO) has been rarely studied in terms of its formation mechanism during the CMD process, compared to carbon nanotube (CNT) or nanofiber (CNF), although CNO has a wide range of potential applications such as supercapacitor electrodes [23], nano lubricants [24], environmental and sensor devices [25].

In specific, the formation mechanism of CNO itself over nickel, which is the most active metal for CMD among the VII transition group [26], has hardly been investigated because the catalyst for generating CNO generally has the shorter reaction time and the lower catalytic activity for CMD than that for generating CNF or CNT. A few studies reported the synthesis of well-organized CNOs over Ni/Al alloy catalysts but CMD was not their main focus [27–29]. Moreover, these prior studies used a high loading of nickel (80 wt.%) to generate CNOs. Unsupported nickel or Ni/Fe alloy catalysts were also used for the synthesis of CNOs, but the catalysts were comparatively unstable and a large amount of nickel was needed to form CNOs considering the characteristics of non-supported catalyst [30–32]. It was recently reported that methane was converted to hydrogen and carbon nano-materials (mostly carbon nanofiber but a small amount of CNO) with a high hydrogen formation rate of more than  $55 \text{ mmol}_{H_2}/(\text{min} \times g_{Ni})$  at  $750^\circ\text{C}$  when Ni–Cu/CNT catalysts were used for CMD [33]. However, the spent catalyst was not considered for re-use, and the cyclic stability of the catalyst for CMD and regeneration was not evaluated.

This study demonstrated unprecedented CMD activity and cycle stability of nickel–carbon composite with  $B_2O_3$  ( $Ni@C-B_2O_3$ ) catalysts derived from  $CO_2$ . In the presence of a small amount of nickel precursor, the catalysts were prepared from  $CO_2$  reaction with  $NaBH_4$ , one of the boron-containing reduction agents based on our previous studies [34–36]. Only pure hydrogen and CNOs were produced under the synthesized  $Ni@C-B_2O_3$  catalyst and none of carbon oxides were detected during CMD. The one-step synthesis of  $CO_2$  carbonization with different amounts of nickel and boron precursors was carried out to investigate the effect of the nickel content on the CMD activity of the catalyst. The catalytic activity of  $Ni@C-B_2O_3$ s for the hydrogen/CNO production was noticeable compared with the recently studied nickel loaded carbon catalysts [33,37] which mainly produced CNT or CNF. The nickel-impregnated boron-doped carbon (Ni/BC) catalyst was also prepared using a conventional method for impregnating boron-doped carbons (BCs) with a nickel precursor. The CMD performance using the  $Ni@C-B_2O_3$  catalyst was compared with that of Ni/BC to understand the effects of the following unique features of  $Ni@C-B_2O_3$  on the activity: (1) the absence of nickel oxide and (2) the amorphous carbon shell structure.

This work elucidated that these unique properties of  $Ni@C-B_2O_3$  led to the high yield of  $CO_x$ -free hydrogen and CNOs. The generation mechanism of hollow metal-free CNOs was proposed on the basis of our experimental findings and the prior two studies [28,32] to understand the unprecedentedly high conversion of methane over the  $Ni@C-B_2O_3$  catalysts. In addition, the cyclic experiment of CMD and catalyst regeneration by  $CO_2$  was also conducted to prove the feasibility of the cyclic process for CMD and  $CO_2$  regeneration, and the morphology of the spent CNO catalyst after a series of cycles was compared with that of the catalyst used once to evaluate the catalytic stability. The carbon support of the catalyst also has merits in view of commercialization such as the tolerance to sulfur and high temperature [38,39], and reducibility of carbon itself [40].  $Ni@C-B_2O_3$  is an environment-friendly catalyst because methane

and  $CO_2$ , two main greenhouse gases, are converted to hydrogen, CNO, and CO by using the  $CO_2$ -derived catalyst.

## 2. Experimental

### 2.1. Chemicals

Sodium borohydride ( $NaBH_4$ ) and nickel nitrate ( $Ni(NO_3)_2 \cdot 6H_2O$ ) were purchased from Sigma-Aldrich. Nickel carbonate ( $NiCO_3$ ) was supplied from Alfa Aesar. Argon (Ar), carbon dioxide ( $CO_2$ ) and methane ( $CH_4$ ) were purchased from Deokyang Co., Ltd. All the chemicals were used as received without further treatments.

### 2.2. Catalyst preparation

$Ni@C-B_2O_3$  catalyst was prepared by the one-step synthesis based on our previous work [41].  $NaBH_4$  was employed as both  $CO_2$  reduction agent and boron precursor while an anhydrous  $NiCO_3$  was selected as a nickel precursor to eliminate the fire safety issue when a nickel precursor is mixed with  $NaBH_4$ . Three different mixtures of 5 g  $NaBH_4$  with 0.25, 0.5, and 0.75 g  $NiCO_3$  were loaded on an alumina crucible boat, respectively, and each crucible was heated from ambient temperature to  $500^\circ\text{C}$  under 76 ml/min (standard temperature and pressure, STP) of  $CO_2$  at a heating rate of  $5^\circ\text{C}/\text{min}$ . After being kept for 2 h at this temperature, the resultant samples were cooled down to room temperature under 76 ml/min (STP) of  $CO_2$ . To remove unreacted mixtures and impurities, the resultant samples were washed with hot deionized water ( $80^\circ\text{C}$ ) for five times, cold deionized water ( $25^\circ\text{C}$ ) for four times, and ethanol ( $25^\circ\text{C}$ ) in turn. After the suspensions were filtered, the cakes were dried at  $120^\circ\text{C}$  overnight. The dried samples were heated in 50 ml/min (STP) of Ar from ambient temperature to  $950^\circ\text{C}$  at a heating rate of  $5^\circ\text{C}/\text{min}$  and calcined at this temperature for 2 h, followed by cooling down. Finally, the resultant catalysts were named as  $xNi@C-B_2O_3$ , where  $x$  is the weight fraction of nickel measured by ICP-OES.

For the comparison purpose, the  $xNi/BC$  catalyst was prepared by the following two synthesis steps: (1) synthesis of BC (boron-doped carbon) using the same procedure as in our previous work [36,42] and (2) subsequent impregnation of a nickel precursor,  $Ni(NO_3)_2 \cdot 6H_2O$  on the BC support.  $Ni(NO_3)_2 \cdot 6H_2O$  was impregnated over BC in deionized water at  $25^\circ\text{C}$  by stirring the mixture for 24 h. Then the mixture was dried at  $120^\circ\text{C}$  overnight, followed by the calcination at  $950^\circ\text{C}$  for 2 h. The same calcination step was employed as in the preparation of  $Ni@C-B_2O_3$ . Finally, the catalyst prepared by the two-step procedure was named as  $xNi/BC$ , where  $x$  is the weight fraction of nickel measured by ICP-OES.

### 2.3. Characterization

Crystalline characteristics of the samples were identified by powder X-ray diffraction (XRD) measurements with D/MAX-2500 X-ray (Rigaku) diffractometer ( $Cu K\alpha$  radiation,  $\lambda = 1.5406 \text{ \AA}$ , 40 kV, 300 mA). X-ray photoelectron spectroscopy (XPS) was performed by Sigma Probe (Thermo VG Scientific) to analyze the chemical structures of the prepared catalysts. The morphologies of catalysts and generated CNOs were observed by a high resolution transmission electron microscope (TEM) with Tecnai TF30 ST (FEI). The elemental dispersive mapping and line profile were collected using Titan cubed G2 60–300 (FEI company). The compositions of synthesized catalysts were measured with inductively coupled plasma optical emission spectroscopy (ICP-OES) in Agilent ICP-OES 720 and Magellan 400 UHR-SEM (at 1 kV) coupled with an energy dispersive X-ray (EDX) spectrometer (OCTANE SUPER, EDAX). Raman spectra of CNOs were measured on ARAMIS (Horiba Jobin Yvon) with Ar ion

**Table 1**  
Compositions of fresh catalysts by ICP-OES and EDX.

Samples	Ni (wt%) <sup>a</sup>	B (wt%) <sup>a</sup>	O (wt%) <sup>b</sup>	C (wt%) <sup>b</sup>
11Ni@C-B <sub>2</sub> O <sub>3</sub>	10.54	7.87	13.60	67.99
13Ni@C-B <sub>2</sub> O <sub>3</sub>	13.39	7.45	14.05	65.11
19Ni@C-B <sub>2</sub> O <sub>3</sub>	18.71	6.23	21.74	56.08
14Ni/BC	14.46	4.78	12.98	67.78

<sup>a</sup> Measured by ICP-OES.

<sup>b</sup> Measured by EDX and normalized with Ni and B contents.

CW laser. The Brunauer–Emmett–Teller (BET) surface area and the pore volume of synthesized catalysts were obtained by nitrogen adsorption at 77 K with 3Flex (Micromeritics).

#### 2.4. Catalytic reactions

Both isothermal and temperature programmed CMDs were performed at atmospheric pressure in a fixed bed reactor (i.d. = 9.8 mm) mounted inside a furnace. In the case of isothermal CMD, 0.10 g of the catalyst was packed between quartz wool layers in the heating zone of the fixed bed reactor. After purging the reactor with N<sub>2</sub>, the reactor was heated from ambient temperature to 750 or 850 °C at a heating rate of 5 °C/min under 40 ml/min (STP) of N<sub>2</sub>. Then the reactant gas of 20 vol.% CH<sub>4</sub> and 80 vol.% N<sub>2</sub> with a total flow rate of 50 ml/min (STP) was introduced for 200 min or 300 min. The product gas was analyzed by an online gas chromatograph (Agilent, 7890B-GC) equipped with a thermal conductivity detector (TCD) and a wet gas meter (Shinagawa, W-NKDa-0.5B), respectively.

The procedure of temperature programmed CMD was similar to that of isothermal CMD except for the heating rate and the time when the reactant gas was introduced. After purging the reactor by N<sub>2</sub>, the reactor was heated from ambient temperature to 200 °C at a heating rate of 4 °C/min under 40 ml/min (STP) of N<sub>2</sub>. Then, a total flow rate of 50 ml/min (STP) with 20 vol.% CH<sub>4</sub> and 80 vol.% N<sub>2</sub> was maintained until the reactor was heated to 900 °C at a heating rate of 4 °C/min.

The cyclic experiment of CMD and CO<sub>2</sub> regeneration for the removal of the carbon deposition was conducted using the same fixed bed reactor. 0.20 g of the catalyst was packed between the quartz wool layers placed in the heating zone of the reactor. After packing the catalyst, the reactor was heated from ambient temperature to 850 °C with a heating rate of 5 °C/min under 40 ml/min (STP) of N<sub>2</sub>. Then, 20 vol.% CH<sub>4</sub> and 80 vol.% N<sub>2</sub> with a total flow rate of 50 ml/min (STP) was introduced for 60 min. Subsequently, the reactor was purged under 40 ml/min (STP) of N<sub>2</sub> at 850 °C until no other gases were detected by the online GC. Next, the CO<sub>2</sub>-N<sub>2</sub> mixture reactant (20 vol% CO<sub>2</sub> and 80 vol% N<sub>2</sub>) with a total flow rate of 50 ml/min (STP) was fed for 60 min to regenerate the spent catalyst from CMD. The cyclic CMD and CO<sub>2</sub> regeneration steps were repeated 15 times.

### 3. Results and discussion

#### 3.1. Formation of boron and nickel oxides (B<sub>2</sub>O<sub>3</sub> and NiO) in Ni@C-B<sub>2</sub>O<sub>3</sub> and Ni/BC

The Ni@C-B<sub>2</sub>O<sub>3</sub> catalysts were synthesized with different amounts of the nickel precursor and their atomic compositions identified by ICP-OES and EDX are shown in Table 1. For the fair comparison of the CMD performance between Ni@C-B<sub>2</sub>O<sub>3</sub> and Ni/BC, the similar amount of nickel in the 13Ni@C-B<sub>2</sub>O<sub>3</sub> catalyst was impregnated on the BC support to prepare 14Ni/BC.

The crystalline structures of xNi@C-B<sub>2</sub>O<sub>3</sub>s shown in Fig. 1 were measured by XRD. The sharp diffraction peaks of Ni@C-B<sub>2</sub>O<sub>3</sub>s at  $\theta = 44.5^\circ$ ,  $51.8^\circ$ , and  $76.4^\circ$  exhibited the characteristic of crys-

**Table 2**

Particle sizes of Ni species in catalysts with different Ni loadings and preparation methods.

	11Ni@C-B <sub>2</sub> O <sub>3</sub>	13Ni@C-B <sub>2</sub> O <sub>3</sub>	19Ni@C-B <sub>2</sub> O <sub>3</sub>	14Ni/BC
Ni (nm)	81.48	79.68	83.38	78.26

talline nickel (JCPDS card No. 87-0712) and no peaks centered at  $\theta = 37.3^\circ$ ,  $43.3^\circ$  and  $62.9^\circ$  indicated the absence of NiO (JCPDS card No. 71-1179) even without a hydrogen-reduction step for the fresh catalyst.

The peaks at  $\theta = 14.6^\circ$  and  $27.8^\circ$  exhibiting B<sub>2</sub>O<sub>3</sub> (JCPDS card No. 06-0297) demonstrated that most of boron and oxygen exist in the form of crystalline boron oxide in Ni@C-B<sub>2</sub>O<sub>3</sub>s.

The XRD pattern of 14Ni/BC shown in Fig. 1 had diffraction peaks indicating the crystalline NiO besides sharp diffraction peaks for nickel metal. Although the reducibility of the carbon support can hinder the generation of NiO during the preparation of 14Ni/BC [43], it could not totally prevent air from oxidizing the nickel particle exposed to the atmosphere, which led to the appearance of a small amount of NiO in 14Ni/BC. However, as observed in the TEM image of 13Ni@C-B<sub>2</sub>O<sub>3</sub> (Fig. 2b), the generation of NiO was suppressed by the well-organized core-shell structure where nickel particles are surrounded by the amorphous carbon. The HAADF STEM and elemental mapping images of 13Ni@C-B<sub>2</sub>O<sub>3</sub> (Fig. 3a, b, and S2) also show that the nickel core is clearly covered by the amorphous carbon shell and then, the oxygen atom is dispersed through the shell, but not aggregated near the nickel core. The HAADF STEM images and line profiles of targeted nickel particles in 13Ni@C-B<sub>2</sub>O<sub>3</sub> are shown in Fig. S3. The length of the carbon profile is longer than that of the nickel profile around the nanoparticle, confirming the core-shell structure of 13Ni@C-B<sub>2</sub>O<sub>3</sub> as previously observed for the general core-shell structure [44–46]. On the contrary, 14Ni/BC displays a partial core-shell structure (Fig. 2d). The HAADF STEM and elemental images of 14Ni/BC (Fig. 3c and d) prove that the nickel particles are exposed to the void although the same operating conditions were set for the elemental mapping of both 13Ni@C-B<sub>2</sub>O<sub>3</sub> and 14Ni/BC. The aggregated oxygen mapping near the nickel particle also supports the presence of NiO in 14Ni/BC. The HAADF STEM images and line profiles of targeted nickel particles in 14Ni/BC (Fig. S4) are clearly different with that of 13Ni@C-B<sub>2</sub>O<sub>3</sub> (Fig. S3), which indicates that the core-shell structure exists only in 13Ni@C-B<sub>2</sub>O<sub>3</sub> and not in 14Ni/BC. Therefore, not only the reducibility of the carbon was responsible for the absence of NiO but the core-shell structure completely hindered the oxidation of nickel in Ni@C-B<sub>2</sub>O<sub>3</sub>s.

No peaks related with boron in the XRD analysis of 14Ni/BC indicated that most of boron exists as an amorphous structure bonded with nickel or carbon. From the weak intensity of the graphite (002) peak at  $\theta = 26.4^\circ$  (Fig. 1) [47] and the absence of graphite layer in TEM images (Fig. 2), it can be surmised that both 13Ni@C-B<sub>2</sub>O<sub>3</sub> and 14Ni/BC have an amorphous carbon structure with a negligible amount of crystalline carbon.

The mean size of nickel particles in both 13Ni@C-B<sub>2</sub>O<sub>3</sub> and 14Ni/BC is in a good agreement with the calculated diameter from Scherrer's equation of XRD patterns shown in Table 2. Due to the absence of the dispersion step, nickel precursors were hardly spread during the preparation of 13Ni@C-B<sub>2</sub>O<sub>3</sub>, thus the size of nickel particles in 13Ni@C-B<sub>2</sub>O<sub>3</sub> has a wide deviation compared to that of 14Ni/BC (Fig. 2a and c). As can be seen in Fig. 2a, nickel particles smaller than 10 nm are neighboring 150 nm of nickel particles in 13Ni@C-B<sub>2</sub>O<sub>3</sub>.

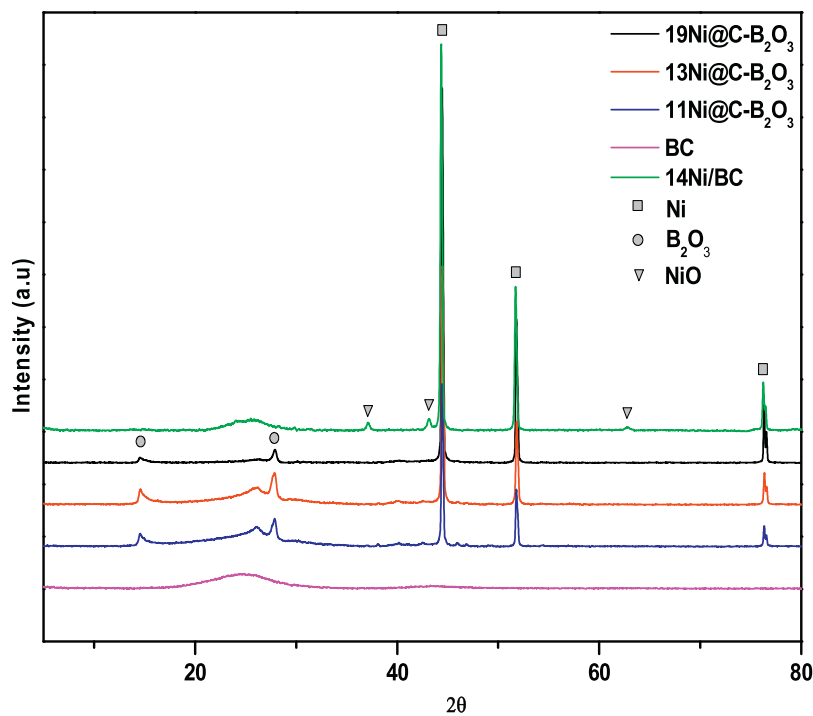


**Fig. 1.** XRD patterns of fresh catalysts.

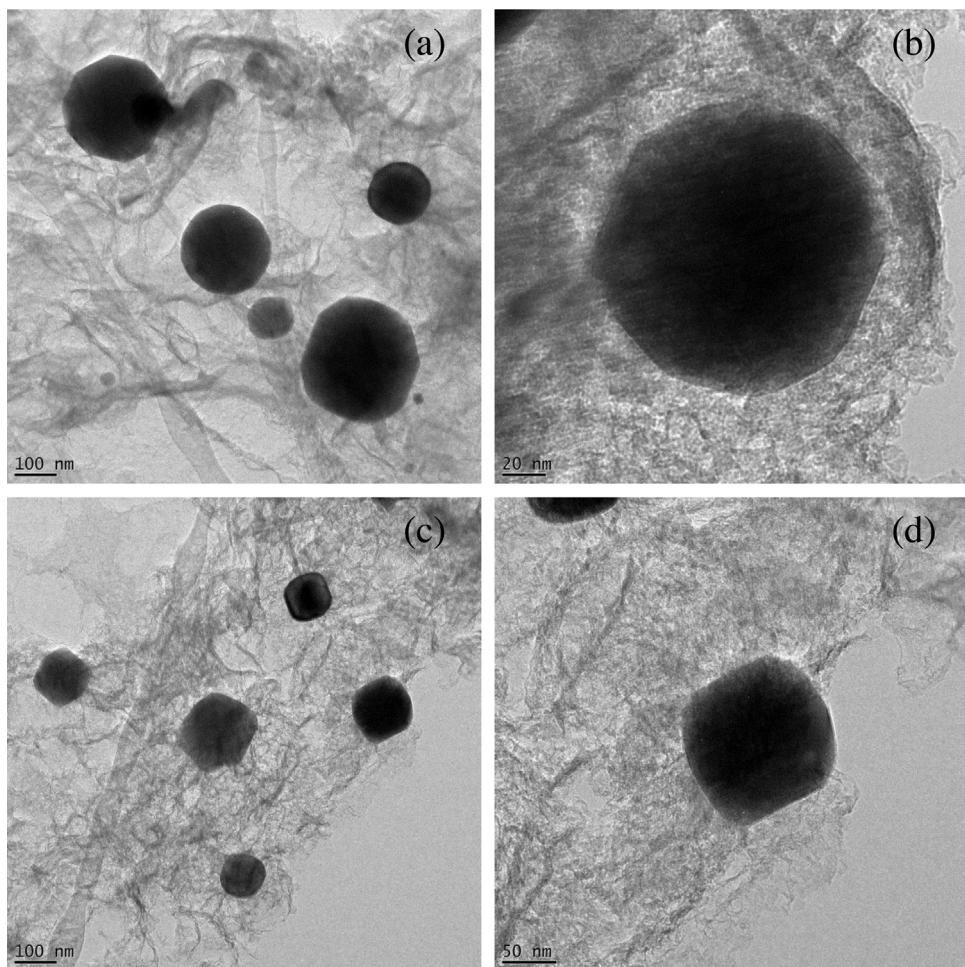


**Fig. 2.** TEM images of fresh catalysts; (a) 13Ni@C-B<sub>2</sub>O<sub>3</sub>, (b) well-organized core–shell structure of 13Ni@C-B<sub>2</sub>O<sub>3</sub>, (c) 14Ni/BC, and (d) partial-organized core–shell structure of 14Ni/BC.

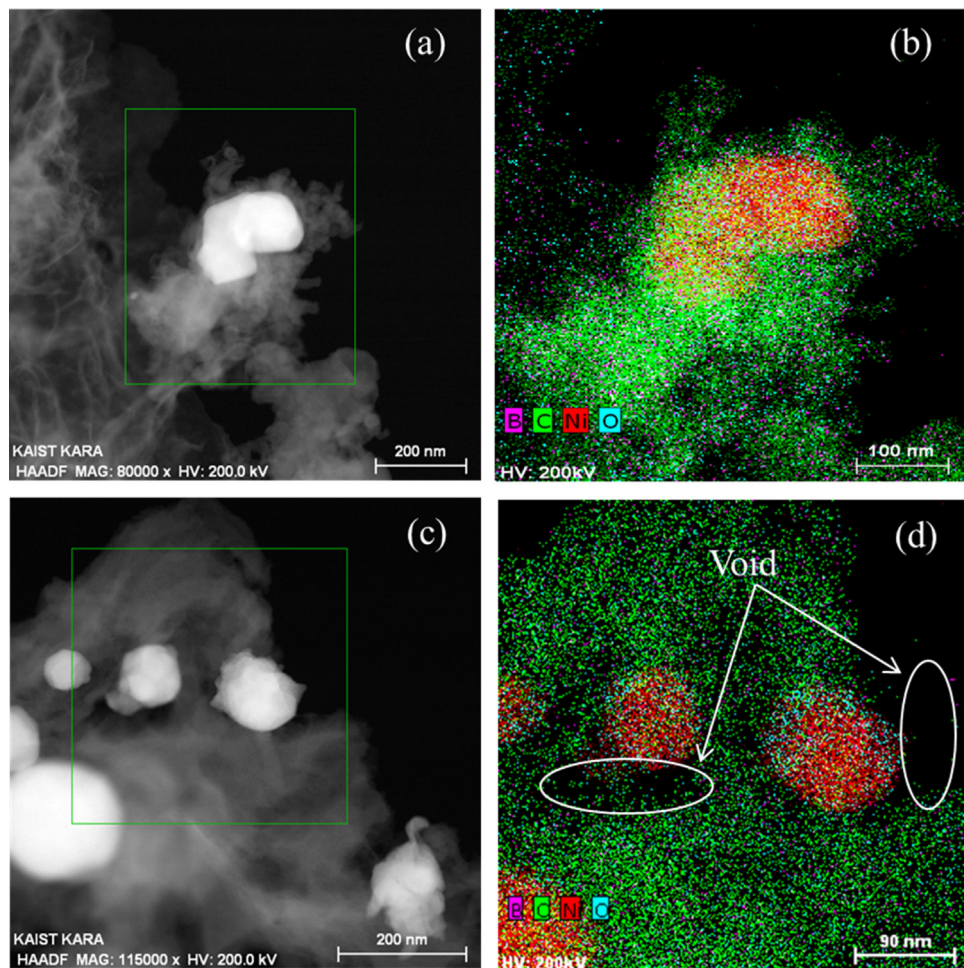


**Fig. 3.** HAADF STEM and elemental mapping images of fresh catalysts; (a) HAADF, (b) elemental mapping of 13Ni@C-B<sub>2</sub>O<sub>3</sub>, (c) HAADF, and (d) elemental mapping of 14Ni/BC.

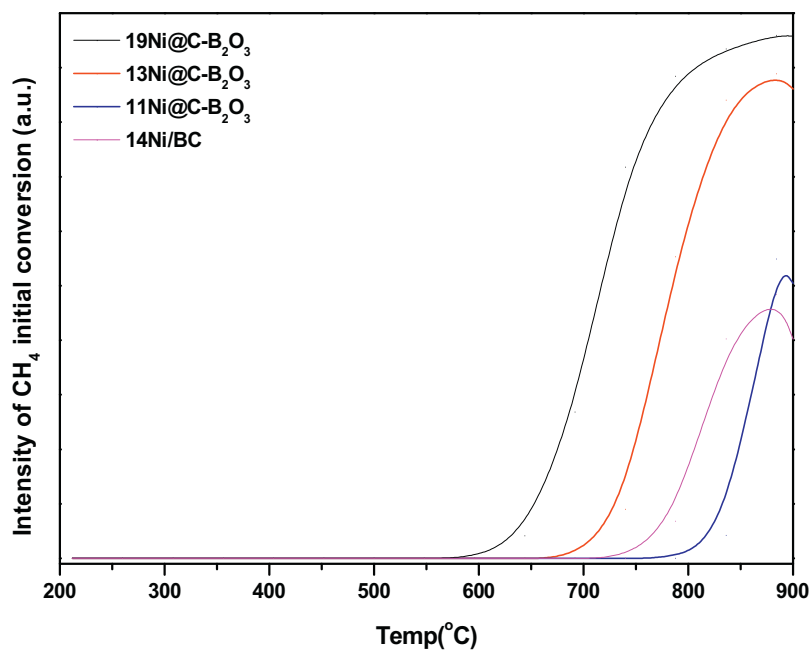


**Fig. 4.** Temperature-programmed CMDs of prepared catalysts.

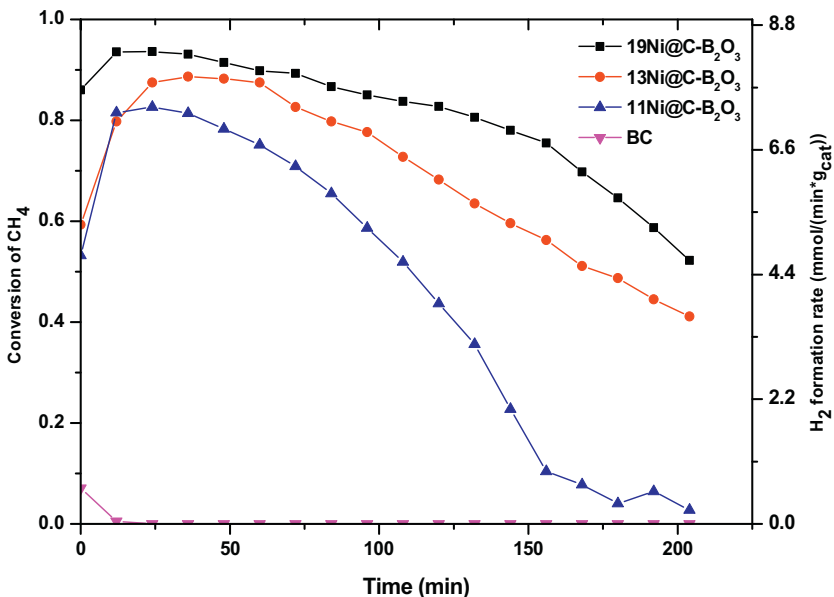


Fig. 5. Isothermal CMDs of catalysts at 850 °C, 30 Lg<sub>cat</sub><sup>-1</sup> h<sup>-1</sup> (CH<sub>4</sub> = 20 vol%).

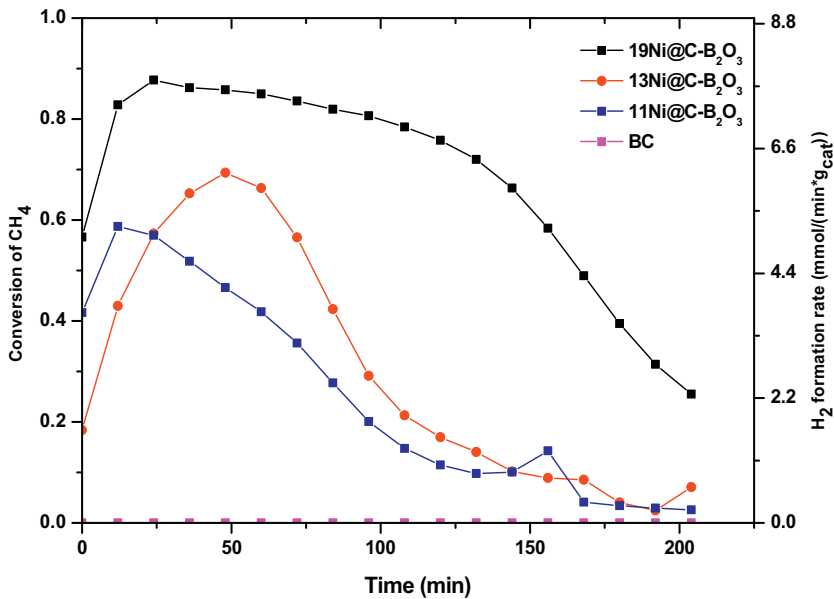


Fig. 6. Isothermal CMDs of catalysts at 750 °C, 30 Lg<sub>cat</sub><sup>-1</sup> h<sup>-1</sup> (CH<sub>4</sub> = 20 vol%).

### 3.2. Temperature programmed and isothermal CMDs of Ni@C-B<sub>2</sub>O<sub>3</sub> and Ni/BC

Fig. 4 shows the results of temperature programmed CMDs. Although a higher metal loaded catalyst was activated at lower temperatures than a lower metal loaded catalyst, the catalytic activities of prepared samples were the highest when the reaction temperature was between 850 and 900 °C. The isothermal CMDs of the Ni@C-B<sub>2</sub>O<sub>3</sub> catalysts at 850 and 750 °C are shown in Figs. 5 and 6. The catalytic activities increased with the raised metal loadings at both 750 and 850 °C. However, as the reaction time went up, they decreased because of the generation of solid carbon deposition. The isothermal CMDs were conducted until the pressure did not exceed 1.08 bars due to the pressure increase caused by the carbon deposition during CMD in a fixed bed reactor. No gaseous products other than hydrogen were observed in the isothermal results of Ni@C-

B<sub>2</sub>O<sub>3</sub>s during CMD. In spite of the small amount of nickel loadings (11–19 wt%), the CH<sub>4</sub> conversion and hydrogen formation rate of the Ni@C-B<sub>2</sub>O<sub>3</sub> catalysts is remarkably high compared with the previous nickel based catalysts for producing CNOs [31–33] and the nickel supported on activated carbon catalyst for generating CNF [37] through CMD as shown in Table 3.

The total carbon yields of Ni@C-B<sub>2</sub>O<sub>3</sub>s are also shown in Table 3 and are compared with the previously reported values [11,48–51]. The prior studies with the high carbon yield focused on producing CNF or CNT instead of CNO and the catalyst for producing CNF or CNT has generally the longer lifespan than the catalyst for producing CNO. Moreover, the carbon yields of most catalysts in Table 3 [48,49,51] were measured until the catalysts were fully deactivated whereas the carbon yields of Ni@C-B<sub>2</sub>O<sub>3</sub>s were obtained only for 200 min and Ni@C-B<sub>2</sub>O<sub>3</sub>s were still active for CMD at the end of run. Despite of the different operating conditions, the average

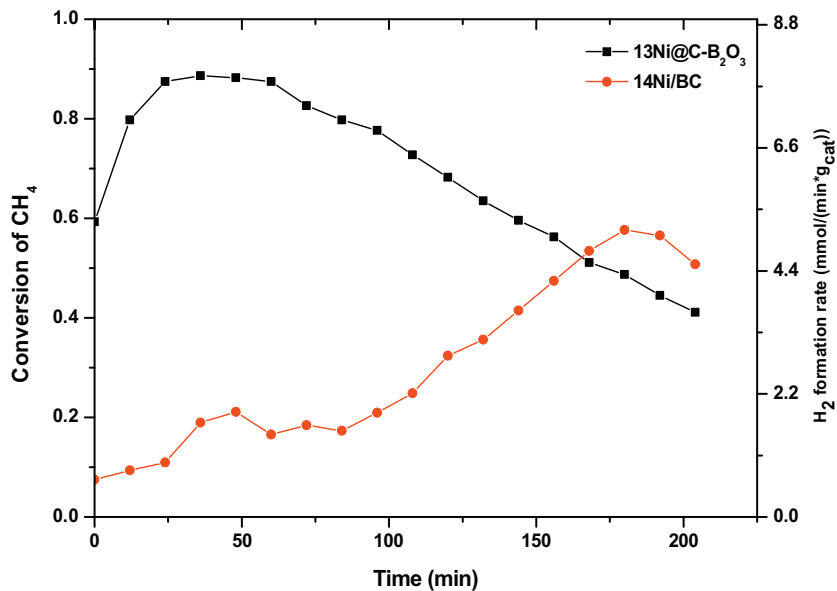


Fig. 7. Isothermal CMDs of 13Ni@C-B<sub>2</sub>O<sub>3</sub> and 14Ni/BC at 850 °C, 30 Lg<sub>cat</sub><sup>-1</sup> h<sup>-1</sup> (CH<sub>4</sub> = 20 vol%).

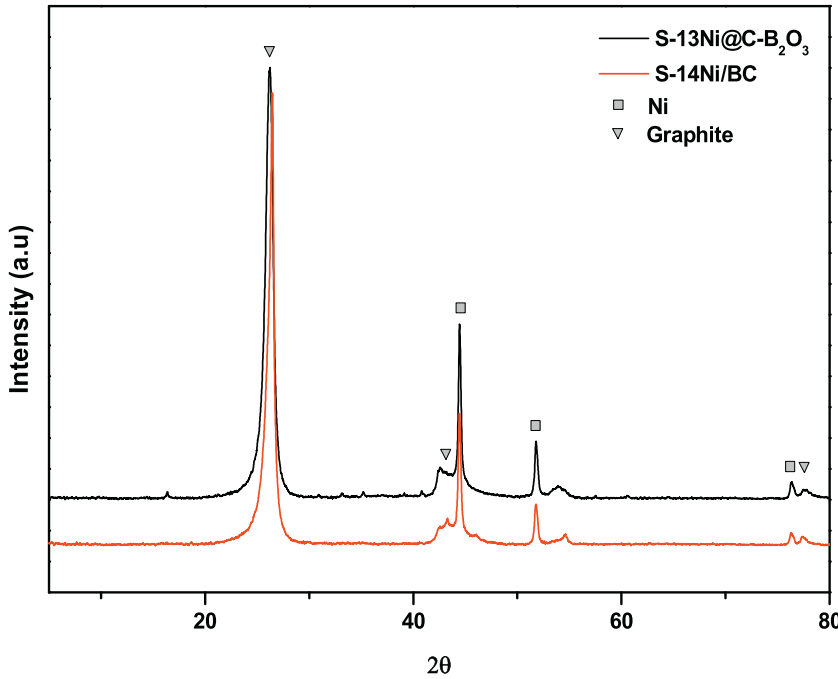
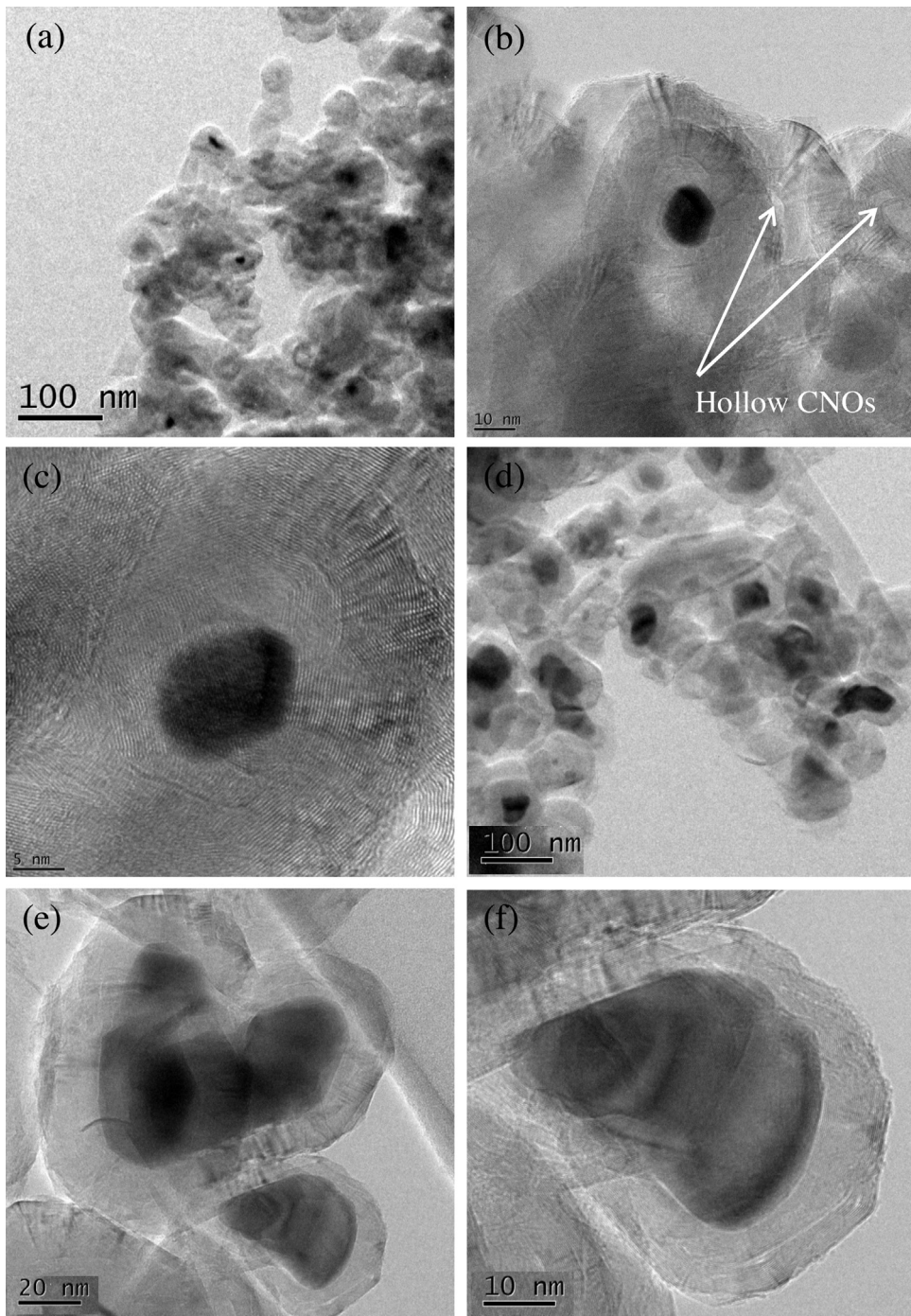


Fig. 8. XRD patterns of S-13Ni@C-B<sub>2</sub>O<sub>3</sub> and S-14Ni/BC.

carbon yield rate of Ni@C-B<sub>2</sub>O<sub>3</sub> is much higher than the previous researches [48–51]. The catalysts which showed the higher total carbon yield due to the longer lifespan [48,49,51] than Ni@C-B<sub>2</sub>O<sub>3</sub> were tested at the lower temperature (500 °C) than Ni@C-B<sub>2</sub>O<sub>3</sub> (700 and 850 °C). Then, the conversions of methane on these catalysts [48,49,51] were less than 0.2, which is much lower than the conversion of Ni@C-B<sub>2</sub>O<sub>3</sub>s. When CMD was conducted at the higher temperature than 500 °C, the lifespans of catalysts were dramatically decreased [48,51]. Specifically, the lifespan of Ni/SiO<sub>2</sub> decreased from 70 to less than 5 h at 700 °C [48] and that of nickel nanoparticle was also decreased from 25 to less than 10 h at 550 °C [51]. Even if the catalysts with the extended lifespans at the low temperature can be used for producing CNF or CNT, the low CH<sub>4</sub> conversions of the catalysts are hardly feasible for the economical

production of hydrogen. Due to the low-purity of hydrogen, additional costs would be required for purifying hydrogen. Although CMD of NiCuAl was conducted 700 °C during 6.25 h [50] which is almost twice as long as the reaction time of Ni@C-B<sub>2</sub>O<sub>3</sub>, the total carbon yield and the average carbon yield rate of NiCuAl were much lower than that of Ni@C-B<sub>2</sub>O<sub>3</sub>. From the over comparison of the carbon yield in Table 3, it can be concluded that Ni@C-B<sub>2</sub>O<sub>3</sub> has the comparable total carbon yield and the improved average carbon yield rate by considering that they were measured during the shorter period at the higher temperature than the reaction temperature in the previous studies [48–51]. BC does not play an active role as nickel does, judging from the unnoticeable activity of BC during CMD at both 750 and 850 °C as exhibited in Figs. 5 and 6.



**Fig. 9.** TEM images of spent catalysts at 850 °C; (a)–(c) S-13Ni@C-B<sub>2</sub>O<sub>3</sub> and (d)–(f) S-14Ni/BC.

Isothermal CMDs of 13Ni@C-B<sub>2</sub>O<sub>3</sub> and 14Ni/BC at 850 °C for 200 min are shown in Fig. 7. Contrary to the previous work [52] that reported the generation of CO<sub>x</sub>-byproducts during CMD, only hydrogen was observed through CMD of 13Ni@C-B<sub>2</sub>O<sub>3</sub>. Because of the small amount of NiO in 14Ni/BC, 838 ppm of CO was detected only at the start of CMD of 14Ni/BC. CH<sub>4</sub>, H<sub>2</sub>, and CO flow rates of isothermal CMDs of 13Ni@C-B<sub>2</sub>O<sub>3</sub> and 14Ni/BC were also shown in Fig. S5. The small amount of NiO was reduced during CMD and there is no XRD peak indicating NiO (Fig. 8) in the spent 14Ni/BC after CMD at 850 °C (S-14Ni/BC). Both XRD patterns of the spent 13Ni@C-B<sub>2</sub>O<sub>3</sub> after CMD at 850 °C (S-13Ni@C-B<sub>2</sub>O<sub>3</sub>) and S-14Ni/BC had a single sharp peaks at  $2\theta = 26.4^\circ$  exhibiting the characteristic of the graphite (0 0 2), which represents the generation of high crys-

talline graphitic layers through CMD. Moreover, the B<sub>2</sub>O<sub>3</sub> peaks of 13Ni@C-B<sub>2</sub>O<sub>3</sub> (Fig. 1) disappeared in the XRD pattern of S-13Ni@C-B<sub>2</sub>O<sub>3</sub> (Fig. 8) because the melting point of B<sub>2</sub>O<sub>3</sub> (450 °C) is much lower than the temperature of CMD (850 °C). The small peaks of S-13Ni@C-B<sub>2</sub>O<sub>3</sub> near  $2\theta = 16, 33, 35$ , and  $41^\circ$  were attributed from the quartz wool, aluminum silicate (JCPDS card No. 62-0481). Because 13Ni@C-B<sub>2</sub>O<sub>3</sub> was packed with the quartz wool before CMD, the small amount of the quartz wool was mixed with S-13Ni@C-B<sub>2</sub>O<sub>3</sub> when recovering it after CMD.

In the results of isothermal CMDs in Fig. 7, the peak point of CH<sub>4</sub> conversion of 14Ni/BC is delayed and then, the maximum CH<sub>4</sub> conversion appears later than the maximum conversion of 13Ni@C-B<sub>2</sub>O<sub>3</sub>. It would be partly due to the small amount of NiO in 14Ni/BC.

**Table 3**

Comparison with previously researched Ni based catalysts.

Researcher	Catalyst	Ni (wt%)	Temp (°C)	$L_{CH_4}/(h \text{ g}_{Ni})$	Maximum H <sub>2</sub> formation rate = $\text{mmol}_{H_2}/(\text{min g}_{Ni})$	$g_C/g_{Ni}$	hr	$g_C/(g_{Ni} \times h)$	Major product
This research	Ni@C-B <sub>2</sub> O <sub>3</sub>	19	850	31.58	44	47	3.33	14	CNO
		19	750	31.58	41	40	3.33	12	CNO
		13	850	46.15	61	59	3.33	18	CNO
		13	750	46.15	47	26	3.33	7.8	CNO
		11	850	54.55	67	47	3.33	14	CNO
		11	750	54.55	47	25	3.33	7.5	CNO
[31]	Ni-Fe	51	850	14		0.576 <sup>a</sup>			CNO
[32]	NiO	100	800	45 <sup>b</sup>	<0.30 <sup>c</sup>				CNO with CNF
[33]	Ni-Cu/CNT	55 <sup>d</sup>	750	45	>55				CNF(major), CNO(minor)
		55 <sup>d</sup>	700	45	>50	614	30	20	CNF
[37]	Ni/AC	20	850	60	>25				CNF/CNT
[48]	Ni/SiO <sub>2</sub>	40	500	225	>25	491	>70	>7	CNF/CNT
[49]	NiO nano		500	90 <sup>b</sup>		398	>75	>5.3	CNF/CNT
[50]	NiCuAl	6.6, 0.12 <sup>e</sup>	700	4 <sup>b</sup>		18	8.33	2.2	CNF/CNT
[51]	NiO nano	32	500	250	>46	302	>25	>12	CNF/CNT

<sup>a</sup> Carbon yield =  $\frac{\text{weight of generated carbon} - \text{weight of reduced catalyst}}{\text{weight of generated carbon}}$  only for [31]. Other carbon yields except [31] are defined and calculated as the ratio of deposited carbon to the mass of metal catalyst ( $g_C/g_{Ni}$ ).

<sup>b</sup>  $L_{CH_4}/(h \times g_{cat})$ .

<sup>c</sup> Methane conversion without H<sub>2</sub> reduction, no activity with H<sub>2</sub> reduction.

<sup>d</sup> Weight fraction including copper (atomic ratio of nickel: copper = 78: 22).

<sup>e</sup> Atomic ratio of Ni/Al = 6.6 and Cu/Ni = 0.12.

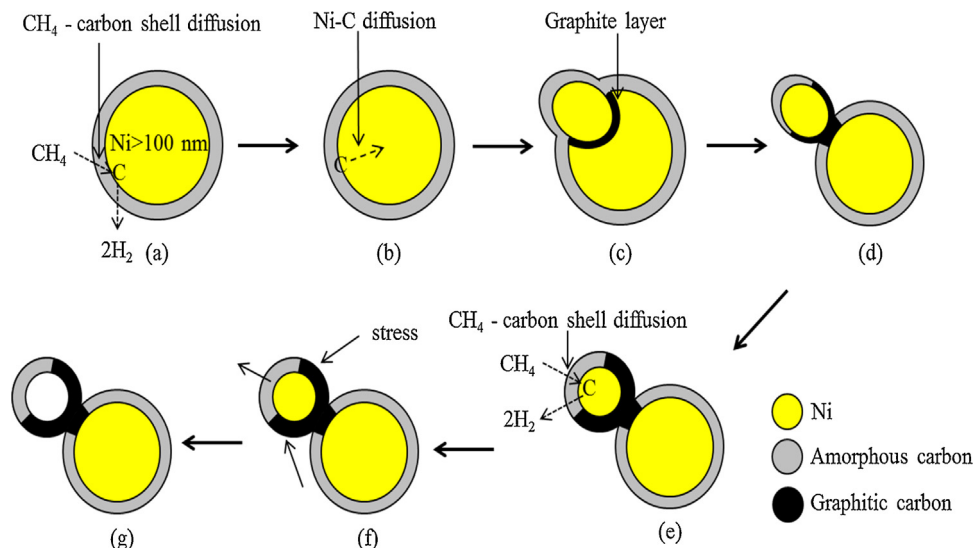


**Fig. 10.** CMD mechanism for generating CNO on Ni@C-B<sub>2</sub>O<sub>3</sub>; (a) methane diffusion and carbon decomposition, (b) carbon diffusion into the large Ni particle, (c) generation of graphite layer inside the large Ni particle, (d) separation of the small Ni fragment, (e) generation of graphite layer on the small Ni fragment (f) escape of the Ni core, (g) generation of the hollow CNO.

However, the CH<sub>4</sub> conversion of 14Ni/BC was still lower than that of 13Ni@C-B<sub>2</sub>O<sub>3</sub> for the whole duration of CMD although all of the NiO was reduced during CMD. The reason for this higher activity of 13Ni@C-B<sub>2</sub>O<sub>3</sub> than 14Ni/BC could be explained by TEM images (Fig. 9) of S-13Ni@C-B<sub>2</sub>O<sub>3</sub> and S-14Ni/BC and the generation mechanism of CNOs in the following section.

### 3.3. Enhanced CMD from the core–shell structure of Ni@C-B<sub>2</sub>O<sub>3</sub>

TEM images of S-13Ni@C-B<sub>2</sub>O<sub>3</sub> and S-14Ni/BC are shown in Fig. 9 and Fig. S6. In both figures, CNOs with quasi-spherical morphology are observed. The inter-planar distance of graphitic carbons is about 0.34 nm which corresponds to the *d*-spacing of the (0 0 2) basal planes in graphite. Encapsulated nickel cores whose sizes are smaller than those of original nickel particles are exhibited at both spent catalysts, which can be explained by the break-down mechanism [32]. According to this mechanism, nickel particles

larger than 100 nm are split into small nickel fragments while generating CNOs during CMD. To be specific, the decomposed carbon from methane is diffused into the large nickel particle at first (Fig. 10b), and then the accumulated carbon inside the large nickel particle forms graphitic layers on the nickel (1 1 1) plane [14] while causing the large nickel particle to split into small nickel fragments (Fig. 10c). After the nickel fragments are generated (Fig. 10d), more methane is decomposed on the surfaces of the fragments. Then CNOs whose nickel cores are smaller than 100 nm are generated during CMD (Fig. 10e).

Whereas CNOs are observed from both S-13Ni@C-B<sub>2</sub>O<sub>3</sub> and S-14Ni/BC, the hollow CNOs without nickel cores are more clearly shown in S-13Ni@C-B<sub>2</sub>O<sub>3</sub> (Fig. 9b) than S-14Ni/BC (Fig. 9e). The generation of the nickel-free hollow CNOs is essential for the higher CH<sub>4</sub> conversion of 13Ni@C-B<sub>2</sub>O<sub>3</sub> than 14Ni/BC because more nickel fragments of 13Ni@C-B<sub>2</sub>O<sub>3</sub> were escaped from the encapsulated CNOs and re-activated for CMD than those of 14Ni/BC.

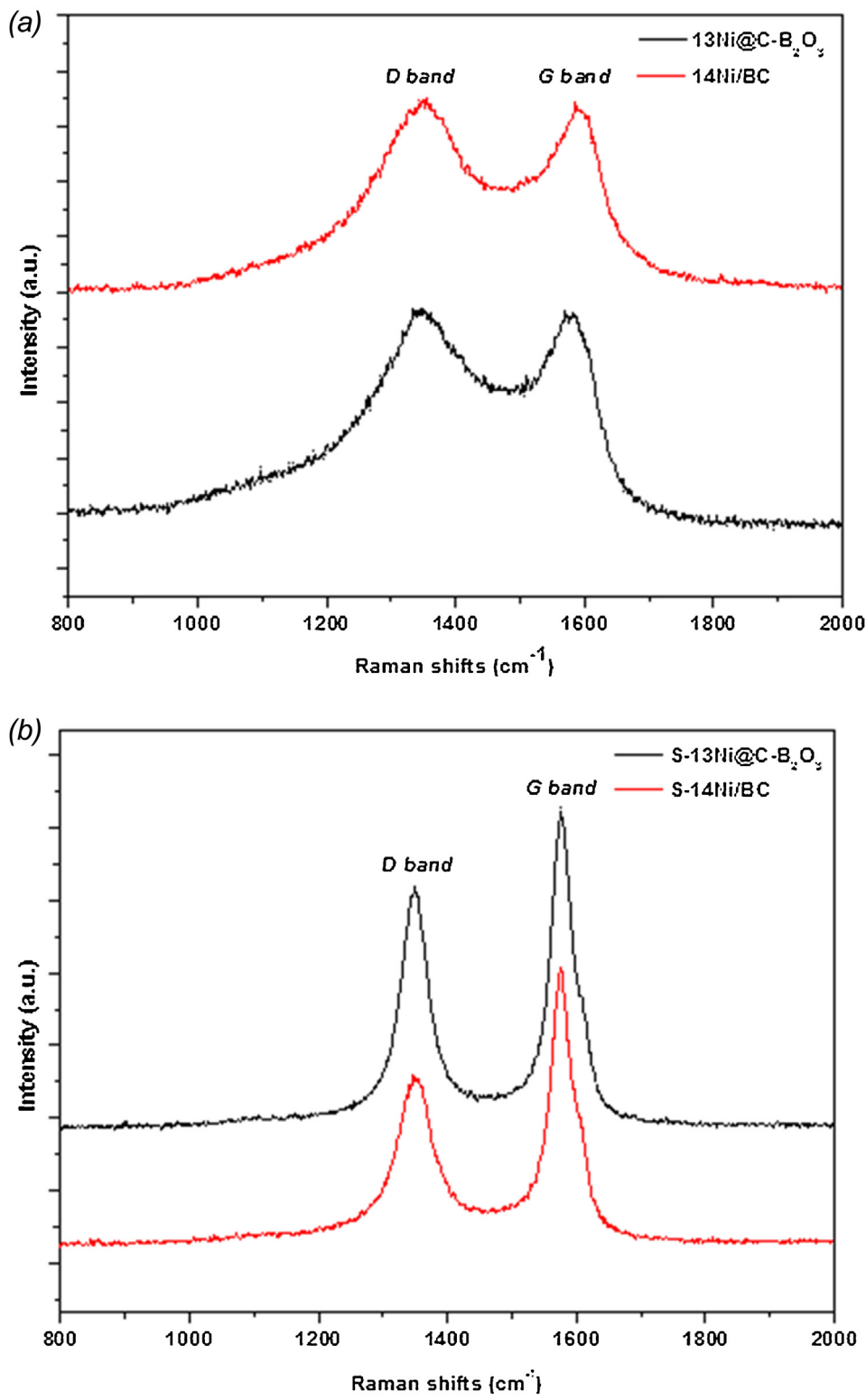


**Fig. 11.** Raman spectra of fresh and spent catalysts; (a) 13Ni@C-B<sub>2</sub>O<sub>3</sub> and 14Ni/BC, (b) S-13Ni@C-B<sub>2</sub>O<sub>3</sub> and S-14Ni/BC.

Before CMD, the large nickel particle of 13Ni@C-B<sub>2</sub>O<sub>3</sub> was covered by the amorphous carbon from the initial core–shell structure when it was prepared at 1 bar of CO<sub>2</sub>. At the initial stage of CMD, methane is adsorbed on the shell and diffused to the nickel surface followed by the decomposition on the nickel surface (Fig. 10a). However, the graphitic crystalline carbon is formed in the nickel phase by the diffusion of the generated carbon into the nickel par-

ticle and then the small nickel fragment is separated from the large nickel particle in a form of CNO (Fig. 10c and d). As a result, parts of carbon encapsulating the small nickel core have the amorphous structure coming from the initial carbon shell, whereas the rest of carbon has the graphitic crystalline structure generated by CMD (Fig. 10e). The encapsulated nickel core is squeezed by the stress of the generated graphitic layers [27,28], which allows the nickel core

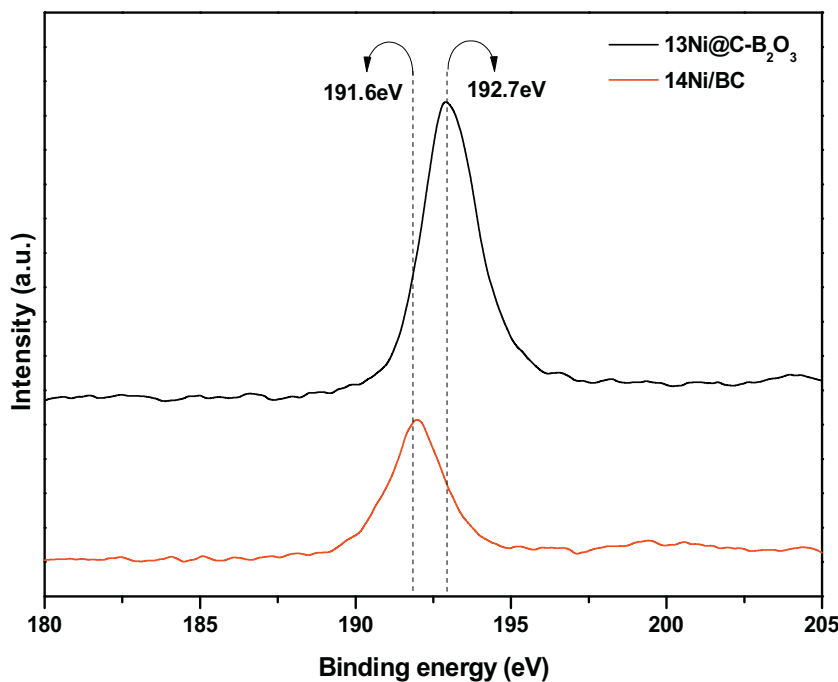


**Fig. 12.** B1s XPS spectra of 13Ni@C-B<sub>2</sub>O<sub>3</sub> and 14Ni/BC.

to be escaped (Fig. 10f). Since it has been previously reported that the small nickel core escapes through the amorphous carbon rather than the crystalline carbon during CMD [28], it can be concluded that the encapsulated nickel core of 13Ni@C-B<sub>2</sub>O<sub>3</sub> is easily escaped from the CNO through the initially existing amorphous part. This escaped nickel core plays an active role in generating another CNO through CMD. The more the hollow nickel-free CNOs are generated (Fig. 10g), the more methane is converted as in the case of 13Ni@C-B<sub>2</sub>O<sub>3</sub>.

On the contrary, in the case of 14Ni/BC, the large nickel core is not fully covered by the amorphous core-shell structure before CMD (Figs. 2 d and 3 c and d), which may not lead to forming CNOs having both amorphous and crystalline graphite carbons. Thus, the nickel core cannot escape easily and a smaller number of hollow CNOs are generated during CMD of 14Ni/BC than that of 13Ni@C-B<sub>2</sub>O<sub>3</sub>, leading to the lower CH<sub>4</sub> conversion. Therefore, the amorphous core-shell structure of 13Ni@C-B<sub>2</sub>O<sub>3</sub> initially derived from CO<sub>2</sub> reduction plays a critical role in providing the high activity through CMD.

Raman spectra of both fresh and spent catalysts also support the generation of CNO with the partially amorphous carbon in S-13Ni@C-B<sub>2</sub>O<sub>3</sub> (Fig. 11). Two broad peaks centered at 1335 cm<sup>-1</sup> and 1585 cm<sup>-1</sup> are named as D and G band, respectively. Whereas D band represents the presence of defective graphite and amorphous carbon [53], G band indicates the carbon–carbon vibration in a two dimensional hexagonal lattice of the graphitic layers [54]. The calculated D and G ratio, indicating the inverse degree of graphitization of generated CNOs, was almost unity in Raman spectra of fresh 13Ni@C-B<sub>2</sub>O<sub>3</sub> and 14Ni/BC (Fig. 11a). After CMD, this ratio is changed to 0.81 for S-13Ni@C-B<sub>2</sub>O<sub>3</sub> and 0.71 for S-14Ni/BC. Although 13Ni@C-B<sub>2</sub>O<sub>3</sub> showed a higher activity for CMD and produced a larger amount of CNOs than 14Ni/BC, the D and G ratio of S-13Ni@C-B<sub>2</sub>O<sub>3</sub> was higher than that of S-14Ni/BC. This clearly indicates that the generated CNO of S-13Ni@C-B<sub>2</sub>O<sub>3</sub> retains a portion of the amorphous carbon originated from the core-shell structure of 13Ni@C-B<sub>2</sub>O<sub>3</sub>, facilitating the escape of the encapsulated nickel core and the high conversion of CH<sub>4</sub>.

### 3.4. Different boron bond in 13Ni@C-B<sub>2</sub>O<sub>3</sub> and Ni/BC

The XPS spectra of B1s at 13Ni@C-B<sub>2</sub>O<sub>3</sub> and 14Ni/BC were measured and compared to analyze the boron bonding. The peak of 13Ni@C-B<sub>2</sub>O<sub>3</sub> at 192.7 eV exhibited the characteristic of B<sub>2</sub>O<sub>3</sub> [55] but the peak of 14Ni/BC at 191.6 eV represented neither pure boron (187.1 eV) nor B<sub>2</sub>O<sub>3</sub> at XPS spectra (Fig. 12). This positively shifted peak of 14Ni/BC from the pure boron peak represented the presence of O–B–C bonding [56].

In NaBH<sub>4</sub> reaction with CO<sub>2</sub>, NaBH<sub>4</sub> was oxidized by CO<sub>2</sub> and then boron derivatives were generated with the formation of sodium salts. All of sodium salts and most of boron derivatives were washed and filtered during the purification step after the reaction. However, the part of boron derivatives still remained after the purification step and existed in the form of B<sub>2</sub>O<sub>3</sub> in 13Ni@C-B<sub>2</sub>O<sub>3</sub> and O–B–C in 14Ni/BC.

The different boron phases in 13Ni@C-B<sub>2</sub>O<sub>3</sub> and 14Ni/BC are coming from the different synthesis methods. It is previously reported that O–B–C was bonded when CO<sub>2</sub> was solely reduced by NaBH<sub>4</sub> [56]. However, the crystalline B<sub>2</sub>O<sub>3</sub> was synthesized during the one-step reaction of CO<sub>2</sub> with NaBH<sub>4</sub> and nickel carbonate precursor.

### 3.5. Stability of Ni@C-B<sub>2</sub>O<sub>3</sub> on a series of CMD and CO<sub>2</sub> regeneration cycles

To confirm the stability of 13Ni@C-B<sub>2</sub>O<sub>3</sub> during the repeated cyclic experiment, a series of CMD and CO<sub>2</sub> regeneration cycles at 850 °C was conducted with 15 L<sub>gcat</sub><sup>-1</sup> h<sup>-1</sup> of 20 vol% CH<sub>4</sub> and CO<sub>2</sub>. The WHSV (weight hourly space velocity) of the cyclic experiment was halved compared with that of the above isothermal and temperature programmed CMDs. Thus, the CH<sub>4</sub> conversion increased over the whole period of CMD (Fig. S7). The WHSV used in the cyclic experiment was still high enough to validate the economic feasibility of 13Ni@C-B<sub>2</sub>O<sub>3</sub> because it was five times more than the previously reported value [57,58].

Different from the previous research [22] regarding the activation step for reducing NiO to nickel after the O<sub>2</sub> regeneration at

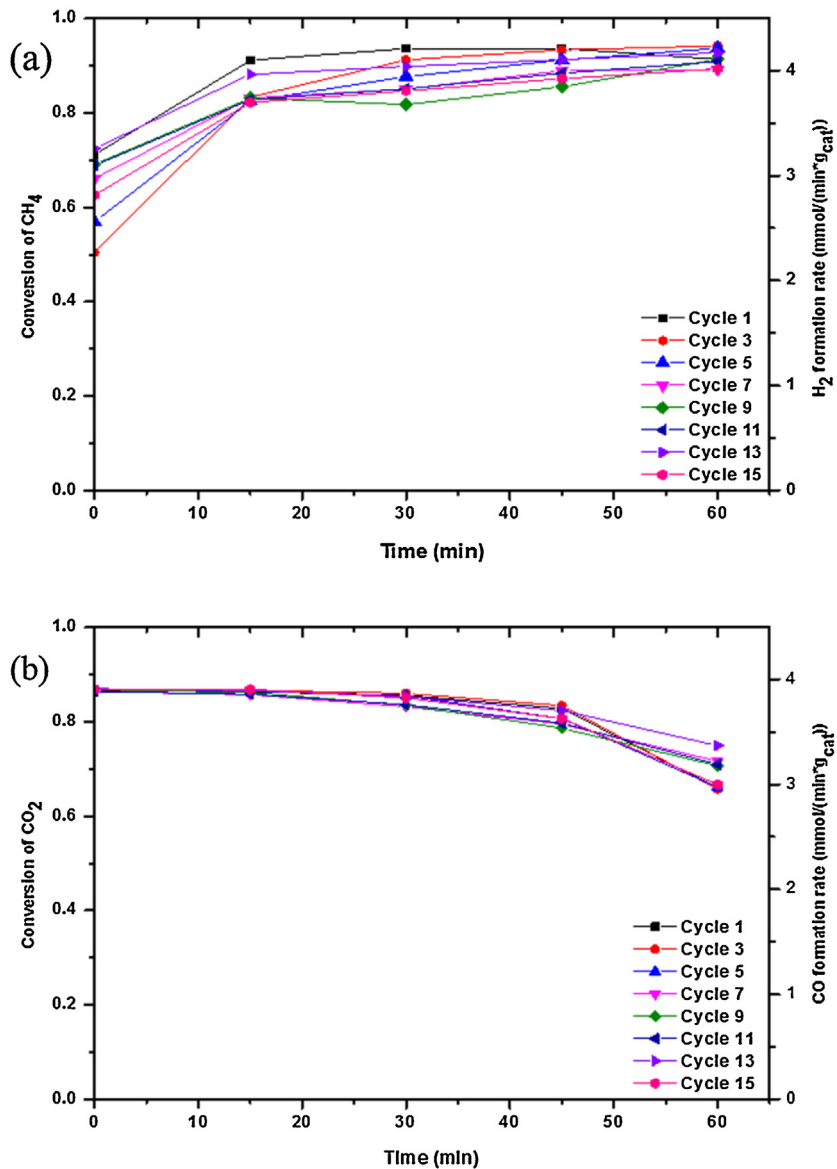


**Fig. 13.** Isothermal CMD and regeneration by CO<sub>2</sub> of 13Ni@C-B<sub>2</sub>O<sub>3</sub> during 15 cycles at 850 °C and 15 Lg<sub>cat</sub><sup>-1</sup> hr<sup>-1</sup> (CH<sub>4</sub> or CO<sub>2</sub> = 20 vol%); (a) CH<sub>4</sub> conversions of CMD, (b) CO<sub>2</sub> conversion of regeneration.

every cycle, our cyclic experiment eliminated this reduction step. Despite of the absence of the activation step, nickel was not oxidized and no gaseous products other than hydrogen were detected from CMD at every cycle because CO<sub>2</sub> was used as the reactant gas at the regeneration step instead of O<sub>2</sub>.

The spent 13Ni@C-B<sub>2</sub>O<sub>3</sub> after CMD was regenerated over 60 min and then the subsequent CMD was conducted on this partially regenerated 13Ni@C-B<sub>2</sub>O<sub>3</sub> because the purity of CO decreases as the regeneration time goes up to fully regenerate the spent 13Ni@C-B<sub>2</sub>O<sub>3</sub>. Despite of the above severe condition, both conversions of CH<sub>4</sub> and CO<sub>2</sub> were stably maintained during 15 cycles (Fig. 13) showing the stability of 13Ni@C-B<sub>2</sub>O<sub>3</sub> for the cyclic process even under the severe operating conditions.

To observe the morphology of the spent catalyst through the cyclic experiment, the part of the regenerated 13Ni@C-B<sub>2</sub>O<sub>3</sub> after the 15th CO<sub>2</sub> regeneration (13Ni@C-B<sub>2</sub>O<sub>3</sub>-15CO<sub>2</sub>) was recovered and the rest of 13Ni@C-B<sub>2</sub>O<sub>3</sub> was used for CMD. Then the spent 13Ni@C-B<sub>2</sub>O<sub>3</sub> after 16th CMD (13Ni@C-B<sub>2</sub>O<sub>3</sub>-16CH<sub>4</sub>) was

recovered. TEM images of both 13Ni@C-B<sub>2</sub>O<sub>3</sub>-15CO<sub>2</sub> and 13Ni@C-B<sub>2</sub>O<sub>3</sub>-16CH<sub>4</sub> are shown in Fig. 14 and Fig. S8. Because the spent catalyst was not fully regenerated, the partial-organized CNOs, and multi wall carbon nanotubes (MWCNTs) are observed in the TEM images of 13Ni@C-B<sub>2</sub>O<sub>3</sub>-15CO<sub>2</sub> (Fig. 14a–c). After the 16th CMD, the number of MWCNTs increases and the graphitic layer of CNOs in 13Ni@C-B<sub>2</sub>O<sub>3</sub>-16CH<sub>4</sub> are thicker than in 13Ni@C-B<sub>2</sub>O<sub>3</sub>-15CO<sub>2</sub> (Fig. 14d–f).

The notable difference between TEM images of S-13Ni@C-B<sub>2</sub>O<sub>3</sub> (Fig. 9a–c) and 13Ni@C-B<sub>2</sub>O<sub>3</sub>-16CH<sub>4</sub> is the presence of MWCNTs generated on the Ni particle whose size is smaller than 70 nm [32,59]. Because the nickel particles larger than 70 nm were split during the 1st CMD to generate CNOs with smaller nickel cores than original ones, the number of nickel particles whose sizes were smaller than 70 nm increased during the repeated cycles. Therefore, more MWCNTs were generated during the 15th CMD than the 1st CMD. Although the morphology of the generated carbon

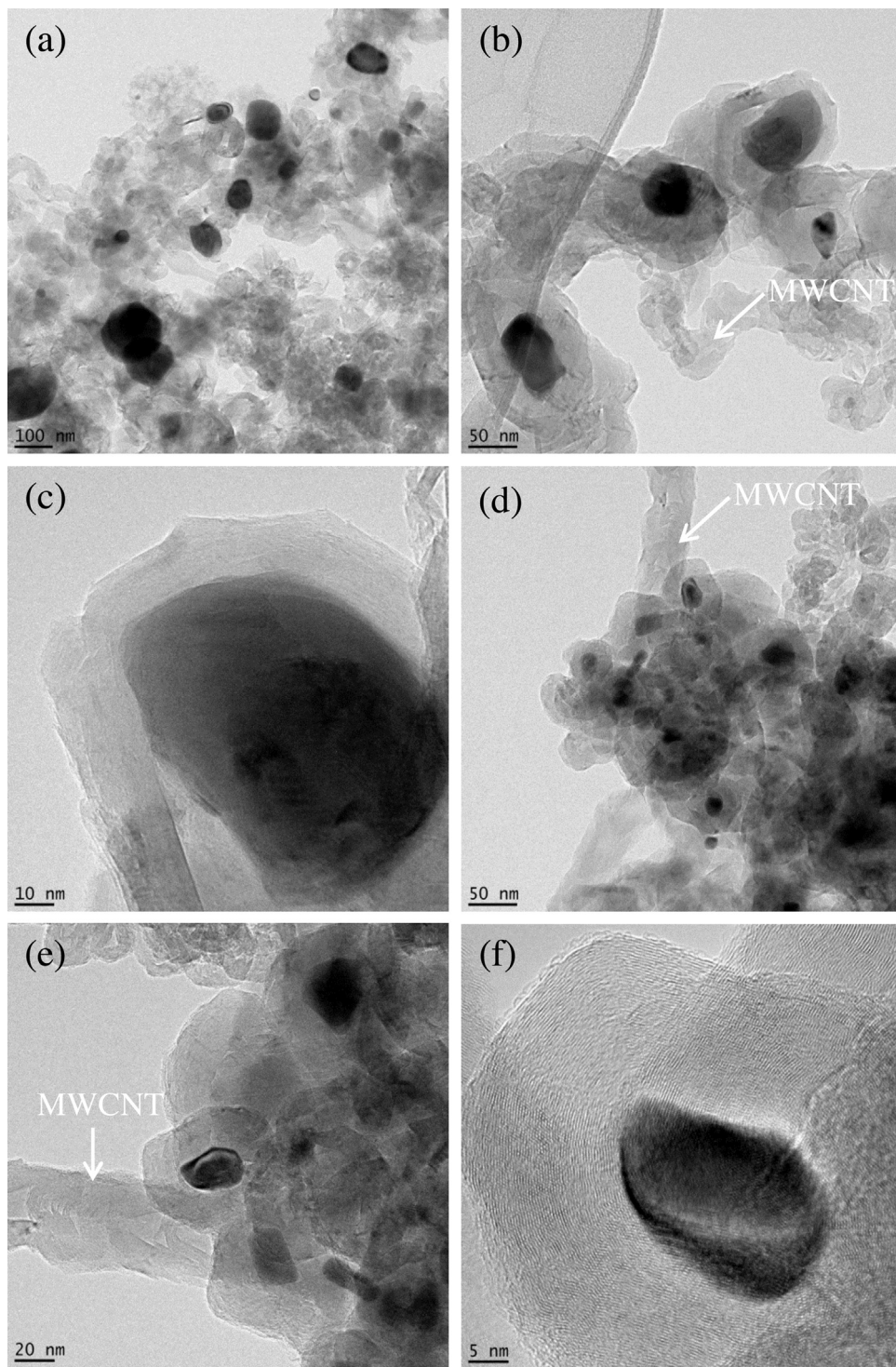


**Fig. 14.** TEM images of the spent Ni@C-B<sub>2</sub>O<sub>3</sub> after the cyclic experiment at 850 °C; (a)–(c) 13Ni@C-B<sub>2</sub>O<sub>3</sub>-15CO<sub>2</sub> and (d)–(f) 13Ni@C-B<sub>2</sub>O<sub>3</sub>-16CH<sub>4</sub>.

was changed through the cyclic operation, the catalytic activity of 13Ni@C-B<sub>2</sub>O<sub>3</sub> was maintained stable during 15 cycles.

#### 4. Conclusions

The one-step reaction of atmospheric CO<sub>2</sub> with NaBH<sub>4</sub> and nickel precursor resulted in nickel–carbon–B<sub>2</sub>O<sub>3</sub> nanocomposite catalysts (Ni@C-B<sub>2</sub>O<sub>3</sub>s). Without any pre-reduction, the synthesized Ni@C-B<sub>2</sub>O<sub>3</sub> was used as the catalyst for CMD at high

temperatures (>750 °C) because the core–shell structure suppressed the generation of nickel oxide. The prepared Ni@C-B<sub>2</sub>O<sub>3</sub> showed a superior catalytic activity for producing hydrogen and CNOs compared to the nickel-impregnated boron-doped carbon catalyst (Ni/BC) synthesized by a conventional impregnation method. The high activity of Ni@C-B<sub>2</sub>O<sub>3</sub> is attributed to the absence of NiO and its amorphous core–shell structure. While generating CNOs, the encapsulated nickel core by carbon deposition was easily escaped through the initial amorphous carbon shell before being

deactivated. The escaped nickel particle was re-used to produce hydrogen and new CNOs while the remaining CNOs without the nickel core were observed in the hollow form. Although the spent Ni@C-B<sub>2</sub>O<sub>3</sub> was partially regenerated by CO<sub>2</sub>, it maintained the stable catalytic activity for CMD during 15 cycles, making Ni@C-B<sub>2</sub>O<sub>3</sub> a practical candidate for the catalyst of the cyclic hydrogen/CO production from the greenhouse gases of methane and CO<sub>2</sub>.

## Acknowledgment

The authors are grateful for the financial support from the Korea CCS R & D Center funded by the Ministry of Science, ICT, and Future Planning (NRF-2014M1A8A1049297).

## Appendix A. Supplementary data

Detail information of BET analysis, TEM images, isothermal CMD, N<sub>2</sub> physisorption, and XPS spectra.

## Appendix B. Supplementary data

Supplementary data associated with this article can be found, in the online version, at <http://dx.doi.org/10.1016/j.apcatb.2015.12.045>.

## References

- [1] U.E.P. Agency, Methane and nitrous oxide emissions from natural sources Washington, DC, USA. (2010).
- [2] S. Dunn, Hydrogen futures: toward a sustainable energy system, *Int. J. Hydrogen Energy* 27 (2002) 235–264.
- [3] D. Li, Y. Nakagawa, K. Tomishige, Methane reforming to synthesis gas over Ni catalysts modified with noble metals, *Appl. Catal. A: Gen.* 408 (2011) 1–24.
- [4] M. Rezaei, S.M. Alavi, S. Sahebdelfar, P. Bai, X. Liu, Z.-F. Yan, CO<sub>2</sub> reforming of CH<sub>4</sub> over nanocrystalline zirconia-supported nickel catalysts, *Appl. Catal. B: Environ.* 77 (2008) 346–354.
- [5] N. Laosiripojana, S. Assabumrungrat, Catalytic dry reforming of methane over high surface area ceria, *Appl. Catal. B: Environ.* 60 (2005) 107–116.
- [6] Y.T. Shah, T.H. Gardner, Dry reforming of hydrocarbon feedstocks, *Catal. Rev.* 56 (2014) 476–536.
- [7] J.K. Hochmuth, Catalytic partial oxidation of methane over a monolith supported catalyst, *Appl. Catal. B-Environ.* 1 (1992) 89–100.
- [8] B. Christian Enger, R. Lødeng, A. Holmen, A review of catalytic partial oxidation of methane to synthesis gas with emphasis on reaction mechanisms over transition metal catalysts, *Appl. Catal. A: Gen.* 346 (2008) 1–27.
- [9] H.F. Abbas, W.M.A.W. Daud, Thermocatalytic decomposition of methane for hydrogen production using activated carbon catalyst: regeneration and characterization studies, *Int. J. Hydrogen Energy* 34 (2009) 8034–8045.
- [10] H.F. Abbas, W.M.A. Wan Daud, Hydrogen production by methane decomposition: a review, *Int. J. Hydrogen Energy* 35 (2010) 1160–1190.
- [11] Y. Li, D. Li, G. Wang, Methane decomposition to CO<sub>x</sub>-free hydrogen and nano-carbon material on group 8–10 base metal catalysts: a review, *Catal. Today* 162 (2011) 1–48.
- [12] U.P.M. Ashik, W.M.A. Wan Daud, H.F. Abbas, Production of greenhouse gas free hydrogen by thermocatalytic decomposition of methane—a review, *Renew. Sustain. Energy Rev.* 44 (2015) 221–256.
- [13] T. Zhang, M.D. Amiridis, Hydrogen production via the direct cracking of methane over silica-supported nickel catalysts, *Appl. Catal. A: Gen.* 167 (1998) 161–172.
- [14] J.I. Villacampa, C. Royo, E. Romeo, J.A. Montoya, P. Del Angel, A. Monzón, Catalytic decomposition of methane over Ni-Al<sub>2</sub>O<sub>3</sub> coprecipitated catalysts: reaction and regeneration studies, *Appl. Catal. A: Gen.* 252 (2003) 363–383.
- [15] K. Otsuka, S. Takenaka, H. Ohtsuki, Production of pure hydrogen by cyclic decomposition of methane and oxidative elimination of carbon nanofibers on supported-Ni-based catalysts, *Appl. Catal. A: Gen.* 273 (2004) 113–124.
- [16] T.V. Choudhary, D.W. Goodman, Stepwise methane steam reforming: a route to CO-free hydrogen, *Catal. Lett.* 59 (1999) 93–94.
- [17] T.V. Choudhary, D.W. Goodman, CO-free production of hydrogen via stepwise steam reforming of methane, *J. Catal.* 192 (2000) 316–321.
- [18] V.R. Choudhary, S. Banerjee, A.M. Rajput, Hydrogen from step-wise steam reforming of methane over Ni/ZrO<sub>2</sub>: factors affecting catalytic methane decomposition and gasification by steam of carbon formed on the catalyst, *Appl. Catal. A: Gen.* 234 (2002) 259–270.
- [19] S. Takenaka, E. Kato, Y. Tomikubo, K. Otsuka, Structural change of Ni species during the methane decomposition and the subsequent gasification of deposited carbon with CO<sub>2</sub> over supported Ni catalysts, *J. Catal.* 219 (2003) 176–185.
- [20] I. Suelves, M.J. Lázaro, R. Moliner, B.M. Corbella, J.M. Palacios, Hydrogen production by thermo catalytic decomposition of methane on Ni-based catalysts: influence of operating conditions on catalyst deactivation and carbon characteristics, *Int. J. Hydrogen Energy* 30 (2005) 1555–1567.
- [21] J.L. Pinilla, I. Suelves, R. Utrilla, M.E. Gálvez, M.J. Lázaro, R. Moliner, Hydrogen production by thermo-catalytic decomposition of methane: regeneration of active carbons using CO<sub>2</sub>, *J. Power Sources* 169 (2007) 103–109.
- [22] M.E. Rivas, C.E. Hori, J.L.G. Fierro, M.R. Goldwasser, A. Griboval-Constant, H<sub>2</sub> production from CH<sub>4</sub> decomposition: regeneration capability and performance of nickel and rhodium oxide catalysts, *J. Power Sources* 184 (2008) 265–275.
- [23] M.E. Plonska-Brzezinska, L. Echegoyen, Carbon nano-onions for supercapacitor electrodes: recent developments and applications, *J. Mater. Chem. A* 1 (2013) 13703–13714.
- [24] Y. Yao, X. Wang, J. Guo, X. Yang, B. Xu, Tribological property of onion-like fullerenes as lubricant additive, *Mater. Lett.* 62 (2008) 2524–2527.
- [25] Y. Li, M. Seymour, Fullerenes and carbon nano-onions for environmental application, in: A. Hu, A. Apblett (Eds.), *Nanotechnology for Water Treatment and Purification*, Springer International Publishing, New York, USA, 2014, pp. 145–158.
- [26] L.B. Avdeeva, T.V. Reshetenko, Z.R. Ismagilov, V.A. Likholobov, Iron-containing catalysts of methane decomposition: accumulation of filamentous carbon, *Appl. Catal. A: Gen.* 228 (2002) 53–63.
- [27] C. He, N. Zhao, C. Shi, X. Du, J. Li, Carbon nanotubes and onions from methane decomposition using Ni/Al catalysts, *Mater. Chem. Phys.* 97 (2006) 109–115.
- [28] C.N. He, C.S. Shi, X.W. Du, J.J. Li, N.Q. Zhao, TEM investigation on the initial stage growth of carbon onions synthesized by CVD, *J. Alloys Compd.* 452 (2008) 258–262.
- [29] C.N. He, F. Tian, S.J. Liu, Z.J. Du, C.J. Liu, F. Li, S.Q. Chen, Characterization and magnetic property of carbon coated metal nanoparticles and hollow carbon onions fabricated by CVD of methane, *Mater. Lett.* 62 (2008) 3697–3699.
- [30] W. Teunissen, F.M.F. de Groot, J. Geus, O. Stephan, M. Tence, C. Colliex, The structure of carbon encapsulated NiFe nanoparticles, *J. Catal.* 204 (2001) 169–174.
- [31] C. Zhang, J. Li, C. Shi, E. Liu, X. Du, W. Feng, N. Zhao, The efficient synthesis of carbon nano-onions using chemical vapor deposition on an unsupported Ni-Fe alloy catalyst, *Carbon* 49 (2011) 1151–1158.
- [32] L. Zhou, Y. Guo, K. Hideo, Unsupported nickel catalysts for methane catalytic decomposition into pure hydrogen, *AIChE J.* 60 (2014) 2907–2917.
- [33] Y. Shen, A.C. Lua, Synthesis of Ni and Ni-Cu supported on carbon nanotubes for hydrogen and carbon production by catalytic decomposition of methane, *Appl. Catal. B: Environ.* 164 (2015) 61–69.
- [34] J.S. Zhang, Y. Zhao, D.L. Akins, J.W. Lee, Thermal decomposition and spectroscopic studies of preheated ammonia borane, *J. Phys. Chem. C* 114 (2010) 19529–19534.
- [35] J.S. Zhang, Y. Zhao, X.D. Guan, R.E. Stark, D.L. Akins, J.W. Lee, Formation of graphene oxide nanocomposites from carbon dioxide using ammonia borane, *J. Phys. Chem. C* 116 (2012) 2639–2644.
- [36] J. Zhang, J.W. Lee, Production of boron-doped porous carbon by the reaction of carbon dioxide with sodium borohydride at atmospheric pressure, *Carbon* 53 (2013) 216–221.
- [37] M. Szymańska, A. Malaika, P. Rechnia, A. Miklaszewska, M. Kozłowski, Metal/activated carbon systems as catalysts of methane decomposition reaction, *Catal. Today* 249 (2015) 94–102.
- [38] N. Muradov, Catalysis of methane decomposition over elemental carbon, *Catal. Commun.* 2 (2001) 89–94.
- [39] N. Muradov, F. Smith, A. T-Raissi, Catalytic activity of carbons for methane decomposition reaction, *Catal. Today* 102–103 (2005) 225–233.
- [40] Z. Bai, H. Chen, B. Li, W. Li, Methane decomposition over Ni loaded activated carbon for hydrogen production and the formation of filamentous carbon, *Int. J. Hydrogen Energy* 32 (2007) 32–37.
- [41] J. Zhang, A. Byeon, J.W. Lee, Boron-doped carbon–iron nanocomposites as efficient oxygen reduction electrocatalysts derived from carbon dioxide, *Chem. Commun.* 50 (2014) 6349–6352.
- [42] J. Zhang, J.W. Lee, Supercapacitor electrodes derived from carbon dioxide, *ACS Sustain. Chem. Eng.* 2 (2014) 735–740.
- [43] J. Zhang, L. Jin, Y. Li, H. Hu, Ni doped carbons for hydrogen production by catalytic methane decomposition, *Int. J. Hydrogen Energy* 38 (2013) 3937–3947.
- [44] M. Heggen, M. Oezaslan, L. Houben, P. Strasser, Formation and analysis of core–shell fine structures in Pt bimetallic nanoparticle fuel cell electrocatalysts, *J. Phys. Chem. C* 116 (2012) 19073–19083.
- [45] K.P. Gong, D. Su, R.R. Adzic, Platinum-monolayer shell on AuNi<sub>0.5</sub>Fe nanoparticle core electrocatalyst with high activity and stability for the oxygen reduction reaction, *J. Am. Chem. Soc.* 132 (2010) 14364–14366.
- [46] L. Gan, M. Heggen, R. O’Malley, B. Theobald, P. Strasser, Understanding and controlling nanoporosity formation for improving the stability of bimetallic fuel cell catalysts, *Nano Lett.* 13 (2013) 1131–1138.
- [47] D. Aurbach, Y. Eineli, The study of Li-graphite intercalation processes in several electrolyte systems using in-situ X-ray-diffraction, *J. Electrochem. Soc.* 142 (1995) 1746–1752.
- [48] S. Takenaka, S. Kobayashi, H. Ogihara, K. Otsuka, Ni/SiO<sub>2</sub> catalyst effective for methane decomposition into hydrogen and carbon nanofiber, *J. Catal.* 217 (2003) 79–87.

- [49] Y. Li, B.C. Zhang, X.W. Xie, J.L. Liu, Y.D. Xu, W.J. Shen, Novel Ni catalysts for methane decomposition to hydrogen and carbon nanofibers, *J. Catal.* 238 (2006) 412–424.
- [50] I. Suelves, M.J. Lazaro, R. Moliner, Y. Echegoyen, J.M. Palacios, Characterization of NiAl and NiCuAl catalysts prepared by different methods for hydrogen production by thermo catalytic decomposition of methane, *Catal. Today* 116 (2006) 271–280.
- [51] H.Y. Wang, A.C. Lua, Development of metallic nickel nanoparticle catalyst for the decomposition of methane into hydrogen and carbon nanofibers, *J. Phys. Chem. C* 116 (2012) 26765–26775.
- [52] J. Li, K.J. Smith, Methane decomposition and catalyst regeneration in a cyclic mode over supported Co and Ni catalysts, *Appl. Catal. A: Gen.* 349 (2008) 116–124.
- [53] A.E. Awadallah, W. Ahmed, M.R.N. El-Din, A.A. Aboul-Enein, Novel aluminosilicate hollow sphere as a catalyst support for methane decomposition to CO<sub>x</sub>-free hydrogen production, *Appl. Surf. Sci.* 287 (2013) 415–422.
- [54] E. Flahaut, F. Agnoli, J. Sloan, C. O'Connor, M.L.H. Green, CCVD synthesis and characterization of cobalt-encapsulated nanoparticles, *Chem. Mater.* 14 (2002) 2553–2558.
- [55] H. Li, H. Li, J.-F. Deng, Glucose hydrogenation over Ni–B/SiO<sub>2</sub> amorphous alloy catalyst and the promoting effect of metal dopants, *Catal. Today* 74 (2002) 53–63.
- [56] J. Zhang, A. Byeon, J.W. Lee, Boron-doped electrocatalysts derived from carbon dioxide, *J. Mater. Chem. A* 1 (2013) 8665–8671.
- [57] V.R. Choudhary, A.M. Rajput, S. Banerjee, Low temperature process for the production of hydrogen, US Patent 6509,000 B1, Jan 21 (2003).
- [58] K.C. Mondal, S. Ramesh Chandran, Evaluation of the economic impact of hydrogen production by methane decomposition with steam reforming of methane process, *Int. J. Hydrogen Energy* 39 (2014) 9670–9674.
- [59] M. Monthioux, L. Noe, L. Dussault, J.C. Dupin, N. Latorre, T. Ubieto, E. Romeo, C. Royo, A. Monzon, C. Guimon, Texturising and structuring mechanisms of carbon nanofilaments during growth, *J. Mater. Chem.* 17 (2007) 4611–4618.